

Numerical study of water depth effects on the hydrodynamic performance of a shallow-water seismic survey ship's Z-drive ducted propeller



Ziyi Ye¹, Shaojuan Su^{*1}, Liangtao Zhou², Zhijie Liu³, Xiaodong Luo²

¹ Naval Architecture and Ocean Engineering College, Dalian Maritime University, 116026, Dalian, Liaoning, China

² Dalian Hengxing Marine Engineering Design Co., Ltd, China

³ Bureau of Geophysical Prospecting (BGP), China National Petroleum Corporation (CNPC), China

ARTICLE INFO

Keywords:

Ka+19A Z-drive ducted propeller

Seismic survey ship

Shallow-water effect

Hydrodynamic performance

ABSTRACT

To meet the propulsion requirements of a novel shallow-water seismic survey ship, a Ka+19A Z-drive ducted propeller was designed based on ship model resistance tests using the propeller chart method. Numerical simulations of open water tests were conducted using Reynolds-Averaged Navier-Stokes (RANS) and transient Rigid Body Motion (RBM) methods, obtaining the open water performance curves. Compared to the original propeller test values, the results verified that the designed propeller could provide effective thrust for the shallow-water seismic survey ship, ensuring its smooth navigation. By varying water depth conditions, the effects of different water depths on the hydrodynamic performance of the Z-drive ducted propeller were investigated, and the influence of shallow-water effects on vortex structures and propeller wake velocity was explored. The results revealed that as the water depth H decreased from deep water to $5D$, the influence on open water performance was minimal. However, as H decreased further from $5D$ to D , significant shallow-water effects emerged, characterized by increases in both the torque coefficient K_Q and total thrust coefficient K_T . Notably, the increase in K_T was more pronounced than that of K_Q , which resulted in an improvement in open water efficiency η_0 . Additionally, the vortex structures and wake velocity demonstrated that the bottom boundary exerted a minimal influence when H decreased from deep water to $2D$, but its effect became pronounced when $H=D$. This study provided guidance for numerical simulation of ducted propellers in shallow-water environments and for propeller design and selection for shallow-water ships.

1. Introduction

When a seismic survey ship operates in shallow water, the performance of the propeller is influenced by the interaction with both the hull and the water bottom. This interaction complicates the flow field around the propeller, thereby reducing propulsive efficiency. Compared with conventional propellers, ducted propellers offer improved propulsive efficiency and mitigate cavitation [1]. Consequently, the novel ship employs a ducted propeller for propulsion.

* Corresponding author.

E-mail address: ssjlpz@dlmu.edu.cn

In recent years, the rapid advancement of computer performance has made numerical calculation methods increasingly favored by researchers. The application of Computational Fluid Dynamics (CFD) methods for predicting the open water performance of propellers has been extensively adopted [2]. Employing CFD to map the open water characteristic curves of ducted propellers allows for accurate predictions of their hydrodynamic performance and facilitates the extraction of detailed flow data surrounding the propulsion device [3]. The Reynolds-Averaged Navier-Stokes (RANS) approach has become a primary method for analyzing fluid dynamic properties and motion. Widely applicable to the characteristics of conventional propellers, these methods are equally applicable to the analysis of ducted propellers.

Hoekstra [4] conducted a hydrodynamic performance study of a ducted propeller system under open-water conditions based on the RANS method, significantly enhancing the accuracy of numerical simulations and providing an important reference for addressing scale effect issues in model tests. Bhattacharyya et al. [5] used the RANS method to study the impact of scale effects on the hydrodynamic performance of ducted propellers. The RANS method demonstrates effectiveness in predicting ducted propeller performance while ensuring computational efficiency, delivering reliable and detailed flow analysis results. Currently, many researchers also integrate the RANS method with other approaches to further improve computational efficiency. For instance, Jin et al. [6] combined the Boundary Element Method (BEM) with the RANS method to compute ducted propeller performance, this coupled approach not only yields prediction results comparable to full RANS simulations but also significantly reduces computational time. Several scholars have also employed Large Eddy Simulation (LES) methods. For example, Zhang et al. [7] proposed a pi-SPDMD model combined with the LES method to capture the turbulent structures in propeller wakes, enhancing the efficiency of sparsity-promoting algorithms in analyzing complex propeller wake flows. Given that the LES method is more suitable for complex flow fields but requires longer computation times, this study employs the RANS method within the STAR-CCM+ software to perform numerical simulations of open water tests for a ducted propeller, validating the effectiveness and reliability of the RANS method in predicting ducted propeller performance.

Currently, three primary methods are employed to study the motion of ducted propellers: the Moving Reference Frame (MRF), the Rigid Body Motion (RBM), and the Overset Mesh (OM). The RBM and OM methods can simulate the actual motion of the propeller and provide a more detailed analysis of the flow field compared to the MRF method. The RBM method exhibits slightly lower accuracy than the OM method, but requires fewer mesh elements, thereby enhancing computational efficiency. Consequently, many researchers currently utilize the RBM method for numerical simulations to analyze the hydrodynamic performance of ducted propellers. For instance, Go et al. [8] used the RBM method to investigate the influence of the duct on propeller performance through numerical simulation. Stark et al. [9] proposed a novel optimized biomimetic marine ducted propeller and applied the RBM method to further analyze the hydrodynamic performance of the ducted propeller. Zhang and Jaiman [10] used the transient RBM method to analyze the wake dynamics characteristics of a ducted propeller, studying parameters such as wake velocity, vortex structure, and pressure distribution under different operating conditions.

Currently, research on the shallow-water effect on propellers primarily focuses on the extent to which water depth influences propeller thrust and torque. However, there is relatively less investigation into how water depth specifically affects the hydrodynamic performance of propellers, particularly concerning the wake velocity, vortex structures, and pressure distribution of ducted propellers. Barrass [11] analyzed the navigational performance in shallow-water under various ship speeds and propeller rotational speeds through numerical simulation and experimental tests. The results indicate that in shallow-water under open water conditions, both ship speed and propeller rotation speed decrease as water depth diminishes. Nakisa et al. [12] investigated the influence of an asymmetrical sloping bank and shallow water on propeller hydrodynamic characteristics, demonstrating that reduced water depth and bank distance significantly enhance thrust and torque, thereby markedly impacting overall propeller performance. Ma et al. [13] investigated the variations of wake fraction near the propeller disk under different water depths and bank distances. Liu et al. [14] utilized the unsteady RANS method and the Volume of Fluid (VOF) model to investigate the impact of underwater propeller wake fields on sedimentation in shallow-water channels.

Current research predominantly focuses on shallow-water effects concerning conventional propellers, with limited attention devoted to ducted propeller performance under shallow-water conditions. Owing to their unique structural configuration, ducted propellers may exhibit distinct hydrodynamic behaviors in shallow-water environments. In this study, numerical simulation is carried out by the RBM method, which not only discusses the influence of water depth on the open water value of ducted propeller but also discusses the influence mechanism of shallow-water effect from the details of wake velocity, vortex structure and pressure distribution. This work provides crucial reference data for optimizing the design and practical deployment of ducted propellers in shallow-water environments.

A novel shallow-water seismic survey ship studied in this study mainly carries out offshore oil exploration. The ship was equipped with a wide and flat bulbous bow, and its main propulsion device adopted a symmetrical double propeller, which could meet the needs of both shallow-water and deep-water operation areas. The shallowest operational water depth was 5 meters [15]. The purpose of this study is to explore the influence of shallow-water on the hydrodynamic characteristics of the Z-drive ducted propeller of the survey ship. Firstly, the propeller blade parameters were designed using the Ka-series propeller chart in conjunction with the ship model resistance tests. The propeller diameter was kept the same as the original propeller, and the Ka+19A Z-drive ducted was obtained by employing the 19A duct. Subsequently, the open water performance of the Z-drive ducted propeller was simulated using the transient RBM method with the STAR-CCM+ 2306.0001 (18.04.009-R8) software. The simulation results were then compared with the test values of the original propeller to validate the accuracy of the computational outcomes. Finally, the total thrust coefficient, torque coefficient, and open water efficiency of the Z-drive ducted propeller under different water depth conditions were calculated. Simultaneously, the pressure distribution on the blade back and blade face, the vorticity structure, and the axial velocity distribution behind the propeller were analyzed and compared under various advance speeds and water depths. Relevant conclusions were drawn from these comparisons, and an in-depth analysis of the influence of shallow-water on the hydrodynamic performance of the Z-drive ducted propeller was conducted. This study provided reference suggestions for subsequent simulation research on ducted propellers under shallow-water conditions and offered valuable insights for the propeller design and selection for shallow-water ships.

2. Propeller design and modeling

2.1 Novel seismic survey ship

The model of the ship is shown in Figure 1, with the main ship parameters listed in Table 1.

Table 1 Principal particulars

Particulars	Value
Length between perpendiculars L_{PP} (m)	84.8
Length on waterline L_{WL} (m)	88.122
Draft molded T (m)	2.82
Depth molded D (m)	5.5
Breadth molded B (m)	16.9
Displacement volume molded ∇ (m ³)	3727.8
Block coefficient C_B	0.922
Wetted surface S (m ²)	1869

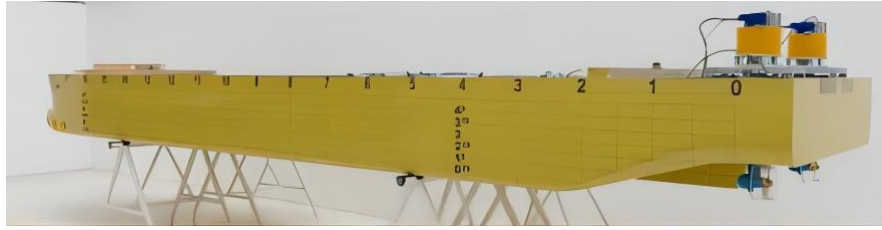


Fig. 1 The model of seismic survey ship

2.2 Propeller design and model building

Propeller design is initially based on the resistance test results of the ship model to calculate the effective power of the actual ship. Subsequently, relevant propulsion factors are selected according to the self-propulsion test results of the ship model. Considering the draft limitations, the propeller diameter is set at 1.65 m, the same as that of the original propeller. The corresponding maximum speed is then determined using the Ka-series propeller charts. Subsequently, cavitation checks, strength assessments, and open water performance curves are performed to obtain the relevant propeller parameters. Finally, the 19A duct and rudder are equipped. The propeller and its model have a scale ratio of $\lambda=11.641$. The essential parameters of the Ka+19A Z-drive ducted propeller and its model are presented in Table 2.

Table 2 Main parameters of Ka+19A Z-drive ducted propeller

Main parameters	Ka+19A Z-drive ducted propeller	Ka+19A Z-drive ducted propeller model
Diameter D (m)	1.65	0.142
Pitch ratio P/D	1.055	1.055
Blade area ratio A_d	0.7	0.7
Inside diameter of duct (m)	1.666	0.143
Tip clearance (mm)	8	0.687
Distance from propeller to rudder shaft (m)	0.715	0.142
Number of blades Z	4	4

The three-dimensional modeling software CATIA is used to complete the modeling of the Ka+19 A Z-drive ducted propeller. The model of the Ka + 19A Z-drive ducted propeller is illustrated in Figure 2.

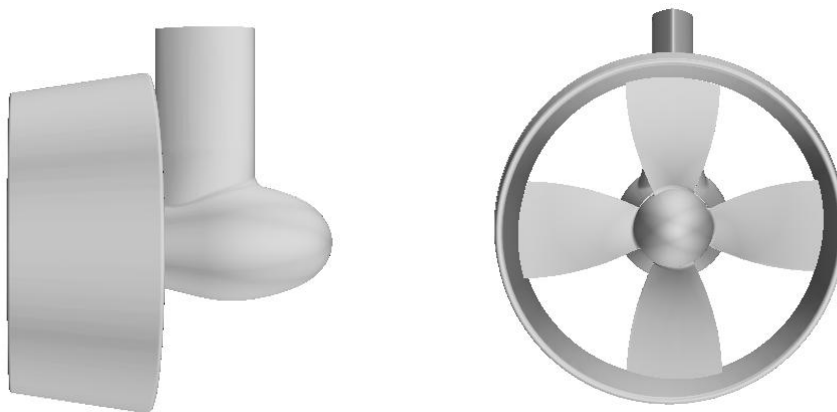


Fig. 2 Model of Z-drive ducted propeller

3. Numerical simulation of open water performance of propeller

3.1 Turbulent flow model

The continuity equation and RANS equation were selected to solve the complex unsteady incompressible turbulent flow [16]. The SST k - ω model, which is widely used for analyzing turbulent flow such as propeller wake, was employed to model the turbulence [17]. The SST k - ω turbulence model was developed to effectively combine the robust and accurate formulation of the standard k - ω model in the near-wall region with the free-stream independence of the standard k - ε model in the far field [18]. The model achieves high calculation accuracy in near-wall free flow, and the application range is expanded by considering the orthogonal divergence term.

The SST k - ω flow equation is presented as follows:

$$\frac{\partial}{\partial t}(\rho k) + \frac{\partial}{\partial x_i}(\rho k u_i) = \frac{\partial}{\partial x_j} \left(\Gamma_k \frac{\partial k}{\partial x_j} \right) + G_k - Y_k + S_k \quad (1)$$

$$\frac{\partial}{\partial t}(\rho \omega) + \frac{\partial}{\partial x_i}(\rho \omega u_i) = \frac{\partial}{\partial x_j} (\Gamma_\omega \frac{\partial \omega}{\partial x_j}) + G_\omega - Y_\omega + D_\omega + S_\omega \quad (2)$$

In the equation: G_k represents the kinetic energy of turbulence; G_ω is the ω equation; Γ_k, Γ_ω are the effective diffusion terms of k and ω ; Y_k, Y_ω are the divergent terms of k and ω ; D_ω is the orthogonal divergence term; S_k, S_ω are given by the user. The effective diffusion equation is shown as follows:

$$\Gamma_k = \mu + \frac{\mu_t}{\sigma_k} \quad (3)$$

$$\Gamma_\omega = \mu + \frac{\mu_t}{\sigma_\omega} \quad (4)$$

where σ_k, σ_ω represent the turbulent Prandtl number of k and ω , respectively.

3.2 Computational domain and mesh division

The computational domain of the Z-drive ducted propeller model comprises a stationary domain and a rotating domain [19]. The stationary domain is obtained by Boolean operation on the external fluid domain, the duct structure and the internal cylinder domain, while the rotating domain is obtained by Boolean operation on the cylindrical domain and the blade. The numerical simulation method for the open water tests of the propeller in this study adopts the transient RBM method. In order to realize the interpolation and transmission of flow field information, an interface must be established between the rotating domain and the stationary domain.

The peripheral computational domain is configured as a cuboid, where the distance from the center of the propeller disk to the top boundary represents the vertical distance from the propeller shaft of the actual ship to the water surface, denoted as h , measuring 0.146 m, with a scale ratio of 11.641. The distances from the center of the propeller disk to the bottom boundary are designated as $5D, 4D, 3D, 2D$, and D , respectively. The distance from the inlet boundary to the center of the propeller disk is $5D$, while the distance from the outlet boundary to the center is $10D$, and the distance from the center of the propeller disk to the side surface is $3D$.

The rotating domain is cylindrical, with the axis of the cylinder aligned with the centerline of the hub. The outlet boundary and inlet boundary of the rotating domain correspond to the outflow and inflow surfaces of the duct, respectively. Computation domain division is shown in Figure 3.

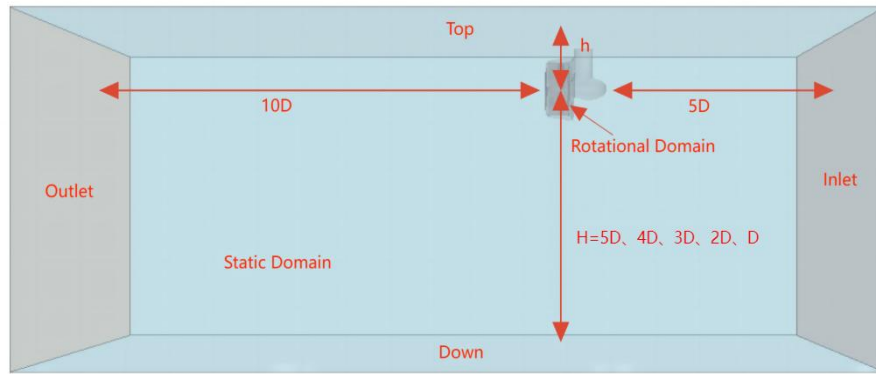


Fig. 3 Computation domain division

The STAR-CCM+ is used for simulations and meshing. In order to decrease the number of grid elements and computational time, a hybrid mesh strategy is employed for the discretization of the region. The rotating domain part adopts the polyhedral mesh, and the external stationary domain adopts the trim mesh [20]. To more effectively capture the characteristics of both the leading edge and trailing edge of the propeller blade, as well as the hub, corresponding feature lines are generated during the geometric processing stage. During the surface meshing, the mesh is refined at the feature line position. To enhance simulation accuracy, a prismatic mesh of uniform size is created on both sides of the interface, effectively addressing the minor gap between the blade tip and the duct. When determining the grid size and prismatic layer around the propeller, ensure that the wall y^+ value is around 1, as shown in Figure 4. In the geometric processing stage, the duct and rudder can also generate feature lines, and the mesh of the feature line position is refined to improve the calculation accuracy. At the same time, prismatic layer grids can be added around the duct and rudder to further optimize the simulation results. To effectively capture the propeller vortex, the grid density behind the propeller is increased. Figure 5 illustrates the grid on the surface of the Z-drive ducted propeller, while Figure 6 shows the grid of the flow field surrounding it.

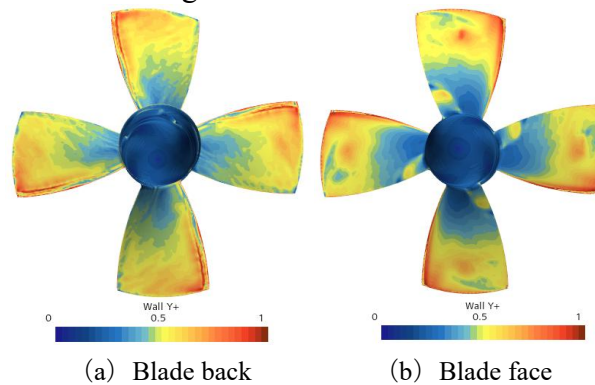


Fig. 4 Blade y^+ value distribution

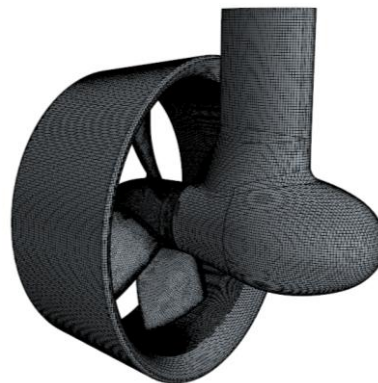


Fig. 5 Surface grid of Z-drive ducted propeller

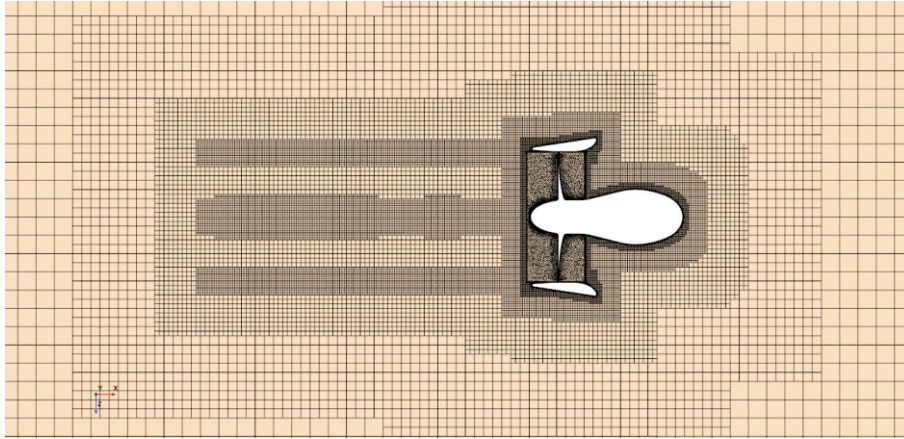


Fig. 6 Flow field grid around Z-drive ducted propeller

3.3 Boundary conditions and solver settings

In this simulation, the water depth of the calculation model is defined as the distance from the center to the bottom of the propeller disk, denoted as H , while the diameter of the propeller is represented as D . Compared to deep water numerical simulations, the bottom in shallow water is a no-slip wall. The boundary condition settings for each operating condition in the numerical simulation are detailed in Table 3.

Table 3 Boundary condition settings

Boundary	$H/D=5, 4, 3, 2, 1$	Deep water
Top	Velocity inlet	Velocity inlet
Down	No-slip wall	Velocity inlet
Inlet	Velocity inlet	Velocity inlet
Outlet	Pressure outlet	Pressure outlet
Side	Velocity inlet	Velocity inlet
Propeller	No-slip wall	No-slip wall
Interface	Interface	Interface

According to the specified conditions and settings, the iterative solution is carried out to obtain the total thrust coefficient K_T , torque coefficient $10K_Q$ and open water efficiency η_0 of the propeller. In this process, the advance coefficient J varies from 0.1 to 0.6. The fluid within the rotating domain is set to rotate clockwise around the propeller shaft at an angular speed of 20 rps, utilizing the transient RBM model. The SST $k-\omega$ turbulence model is employed for turbulence simulation, with water properties set at a temperature of 19 °C, a density of 998.4 kg/m³, and a kinematic viscosity of 1.028E-06 m²/s. In this study, the SIMPLE algorithm solver is used to solve the pressure-velocity coupling equation. The convection term is discretized by the upwind scheme with second-order accuracy, the diffusion term is discretized by the central difference scheme, and the time term is discretized by the Euler implicit discrete scheme with first-order accuracy.

3.4 Numerical verification method

Following the numerical simulation verification methods outlined by Stern [21] and Wilson [22], a grid size convergence analysis is performed under deep water conditions at $J=0.2$. A CFD uncertainty analysis of the hydrodynamics of the propeller in open water is conducted to evaluate and validate the reliability of the numerical simulation method.

The accuracy of the numerical results mainly depends on the grid size. Generally, smaller grid sizes can capture finer features of the flow field, thereby enhancing the precision of the calculations. However, excessively small grid sizes can significantly increase computational costs, making it necessary to strike an appropriate balance when selecting grid size. According to the regulations recommended by ITTC [23], the

difference between the calculation results of two adjacent discrete parameters can be expressed as ε . where S_i represents the numerical computation result, and R represents the convergence rate, and its expression is:

$$R = \frac{\varepsilon_{21}}{\varepsilon_{32}} = \frac{S_2 - S_1}{S_3 - S_2} \quad (5)$$

Based on the obtained convergence rate R , it can be judged that there may be three cases of convergence: if $R < 0$, it indicates oscillatory convergence; if $0 < R < 1$, it indicates monotonic convergence; if $|R| > 1$, it indicates divergence.

When conducting a grid size convergence analysis, the grid base size encryption ratio is set to $r = \sqrt{2}$, and three sets of grids, Coarse (S_1), Medium (S_2), and Fine (S_3) are established, with their total number of elements being 2.22 million, 3.39 million and 6.12 million respectively. Simultaneously, the time step for all three grid sets is maintained at $t=0.00027$ s, with other settings remaining unchanged. Similarly, in the study of time step convergence, the medium grid S_2 is selected, and the time step is gradually increased by the growth rate $r = 2$, and the three groups of different time steps of T_1 , T_2 and T_3 are respectively configured for comparative calculation. Following ITTC recommendations [24], the rotating propeller, a minimum of 180-time steps per revolution is utilized, and the time step of $T_2=0.00027$ s is selected, with other settings remaining unchanged. At advance coefficient $J=0.2$, based on the given conditions and the grid size and time step convergence analysis conducted, uncertainty analysis results for K_T , $10K_Q$, and η_0 can be obtained, as shown in Tables 4 and 5.

Table 4 Grid convergence and uncertainty analysis results

$J=0.2$	S_1	S_2	S_3	R_G	P_G	δ_G	$\delta_G(\%D)$	U_G	$U_G(\%D)$
K_T	0.4369	0.4357	0.4352	0.647	1.257	-0.002	-0.390	0.0009	0.177
$10K_Q$	0.4923	0.494	0.4951	0.417	2.527	0.000	0.082	0.0001	0.033
η_0	0.2832	0.281	0.28	0.455	2.276	0.001	0.311	0.0002	0.062

Table 5 Time step convergence and uncertainty analysis results

$J=0.2$	T_1	T_2	T_3	R_T	P_T	δ_T	$\delta_T(\%D)$	U_T	$U_T(\%D)$
K_T	0.4369	0.4357	0.4352	0.667	1.17	0.000320	0.062	0.00016	0.031
$10K_Q$	0.4923	0.494	0.4951	0.2	4.646	-0.000004	-0.001	0.00001	0.003
η_0	0.2832	0.281	0.28	0.25	4.002	-0.000013	-0.005	0.00003	0.01

According to the given data analysis results, the grid convergence rates R_G of the K_T , $10K_Q$, and η_0 are 0.647, 0.417, and 0.455, respectively, all between 0 and 1, indicating that the grid convergence is monotonous. The grid numerical discrete uncertainty U_G is 0.177 %D, 0.033 %D and 0.062 %D, respectively, showing a relatively small error. The error of grid S_1 is slightly larger, and of grid S_3 is too much, resulting in a longer calculation time.

The time step convergence analysis shows that the time step convergence rate R_T of the K_T , $10K_Q$, and η_0 are 0.667, 0.2, and 0.25, respectively, which also satisfy the monotonic convergence condition. The time step discrete uncertainty U_T is 0.031 %D, 0.003 %D, and 0.01 %D, which are also in the acceptable range. By comparing the calculation results of the three time steps, it is found that appropriately reducing the time step can improve accuracy but reduce computational efficiency.

According to the above comprehensive consideration of the balance between calculation accuracy and efficiency, the grid S_2 and time step $t=0.00027$ s are finally selected to carry out subsequent numerical simulation research.

3.5 Analysis of open water calculation results

The open water test data for the original propeller model of the ship comes from testing the large DP shallow-water seismic survey ship "Innovator" at the MARIN deep-water towing tank in the Netherlands, as shown in Figure 7.



Fig. 7 Deep water towing tank

Table 6 shows the open water performance data of numerical simulation and experiment. The simulation results of the K_T , $10K_Q$, η_0 and advance coefficient J of the Z-drive ducted propeller have been given:

$$J = \frac{V_A}{nD} \tag{6}$$

$$K_T = \frac{T}{\rho n^2 D^4} \tag{7}$$

$$K_Q = \frac{Q}{\rho n^2 D^5} \tag{8}$$

$$\eta_0 = \frac{K_T J}{K_Q 2\pi} \tag{9}$$

where D represents the propeller diameter (m), n denotes the propeller rotational speed (rps), Q is the propeller torque (Nm), T is the total thrust generated by the propeller, duct, and rudder (N), V_A is the propeller advance speed (m/s), and ρ is the water density.

Table 6 Open water performance data

J	Experimental			CFD		
	K_T	$10K_Q$	η_0	K_T	$10K_Q$	η_0
0.1	0.4952	0.5326	0.148	0.4932	0.5055	0.1554
0.2	0.435	0.5165	0.268	0.4357	0.494	0.281
0.3	0.3759	0.4947	0.363	0.379	0.4773	0.3793
0.4	0.3191	0.4661	0.436	0.3236	0.4545	0.4535
0.5	0.2632	0.4297	0.487	0.2711	0.4265	0.5061
0.6	0.2054	0.3844	0.51	0.216	0.3883	0.5315

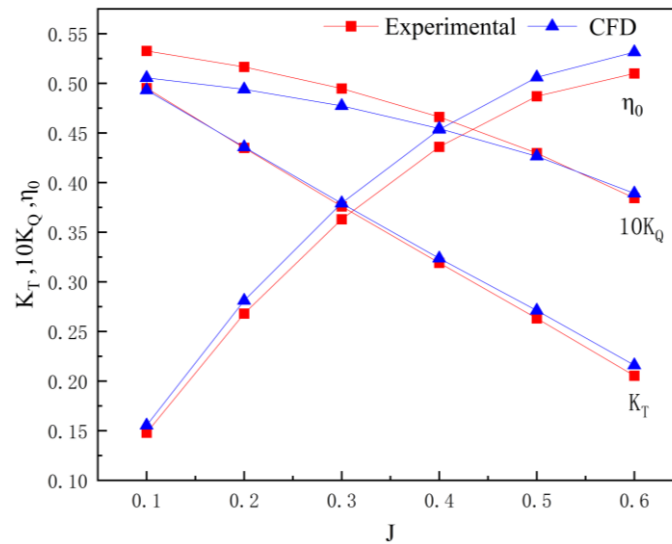


Fig. 8 Open water characteristic curve

According to the open water characteristic curve of the Z-drive ducted propeller illustrated in Figure 8, it is evident that the open water performance of the Ka+19A Z-drive ducted propeller shows a good agreement between the numerical simulation results and the original propeller test data [25]. In the advance coefficient range of $J=0.1-0.6$, the average relative error of the calculated $10K_Q$ for the propeller is approximately 2.86 %, with a maximum relative error of 5.09 %. The average error of K_T is about 1.82 %, and the maximum error is 5.16 %. The average relative error of the η_0 is around 4.41 %, with a maximum relative error of 5 %. Although the numerical results show slight discrepancies from the experimental data, they exhibit a similar trend [26].

Figures 9 and 10 illustrate the pressure distribution cloud diagrams for the entire Ka+19A Z-drive ducted propeller and the duct when the advance coefficient is $J= 0.2$. The pressure distribution on the rudder is relatively uniform, gradually decreasing from the front to the rear, which aids in generating thrust. The pressure distribution outside the duct is also relatively uniform, while the internal pressure distribution is uneven and the gradient is large. The pressure on the inner wall of the duct near the propeller is low. This is due to the high water velocity at the blade tip clearance, creating a notable low-pressure zone at the propeller blade tip [27]. The pressure on the inner wall of the duct gradually increases from the middle area near the propeller to the front and rear ends, and the pressure on the front end of the inner wall of the duct is smaller than that on the rear end. In general, the pressure on the inner wall of the duct is less than that on the outer wall, which is also the reason for the thrust of the duct. The total thrust of this propeller consists of propeller thrust, duct thrust, and rudder thrust.

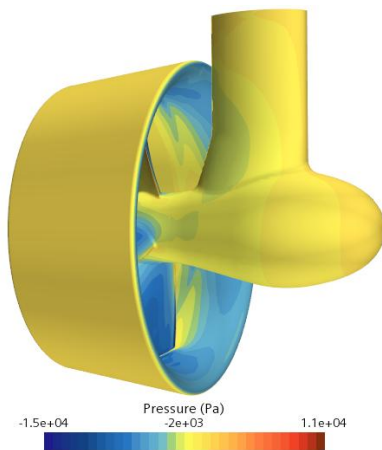


Fig. 9 Pressure distribution of Z-drive ducted propeller

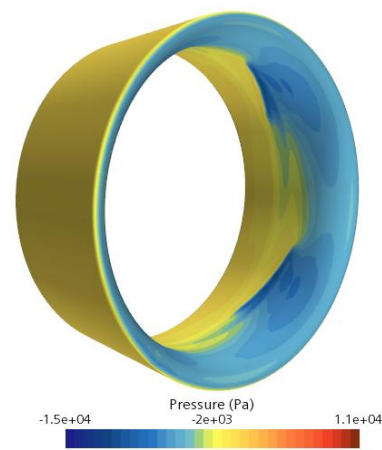


Fig. 10 Pressure distribution of duct

Figure 11 (a) to (f) and Figure 12 (a) to (f) are the pressure distribution of the Z-drive ducted propeller blade back and blade face under the $J=0.1-0.6$, respectively. Under the same advance coefficient, the blade back is the suction surface, which mainly presents the negative pressure area. The pressure at both the leading edge and trailing edge is higher than that in the central region, with pressure gradually decreasing from the root to the tip of the blade, resulting in a significant change in pressure distribution gradient. Conversely, the blade face serves as the pressure surface, where the pressure at the leading and trailing edges is also greater than that in the middle area. Pressure increases from the blade root to the tip, displaying a smaller gradient in the pressure distribution. In general, the overall pressure of the propeller blade back is lower than the blade face, creating a pressure difference that generates forward thrust.

With the increase in the J , the pressure on the blade back also rises, particularly in the middle region where the pressure shows a significant increase. Meanwhile, the pressure distribution on the blade face changes minimally, and surface pressure decreases as the J grows. Although the blade back pressure remains lower than the blade face pressure, the pressure difference between the two narrows as the J increases. This reduction in pressure difference leads to a decrease in thrust, consistent with the results shown in Figure 7.

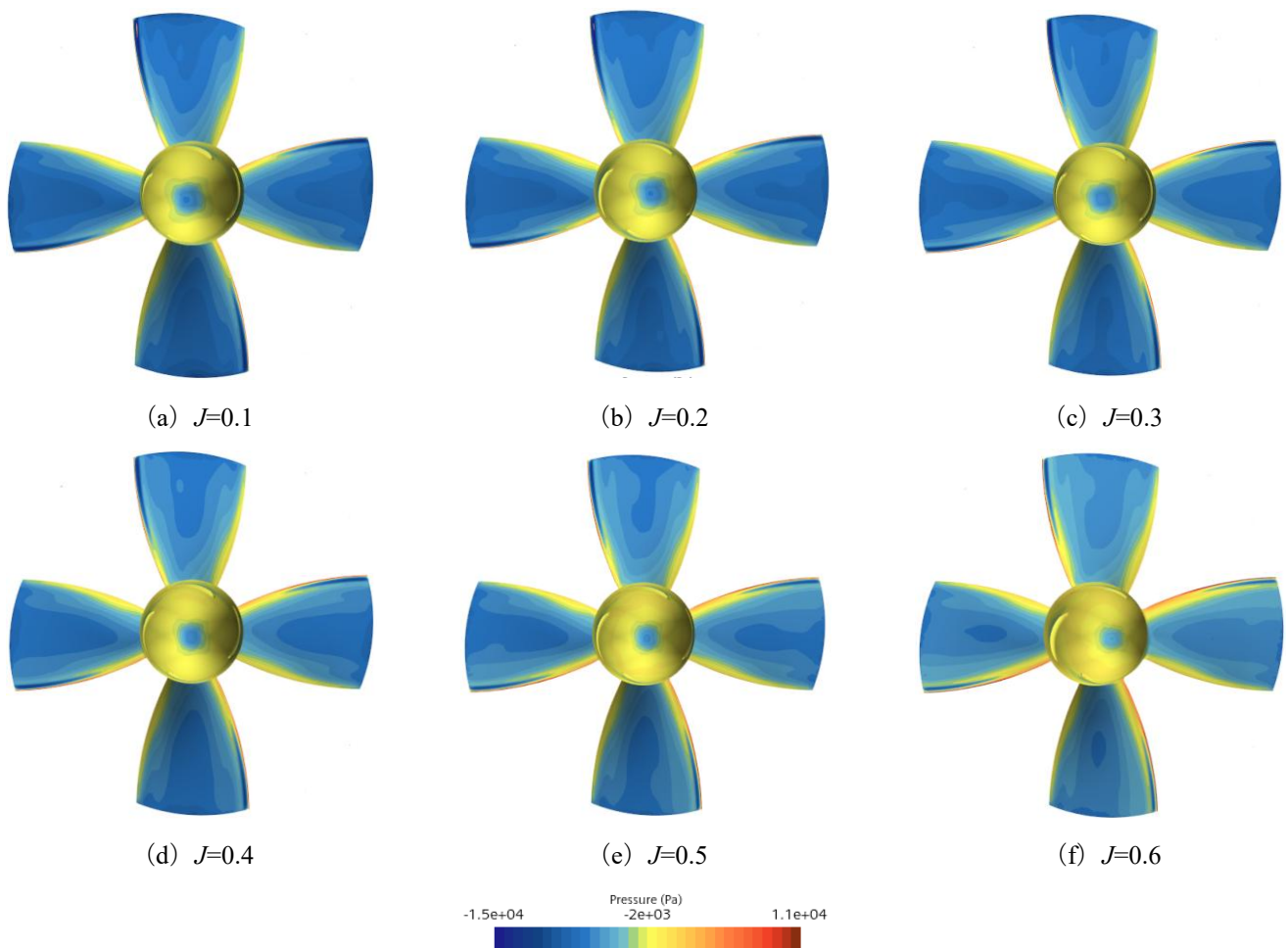


Fig. 11 Pressure distribution on blade back under different advance speeds

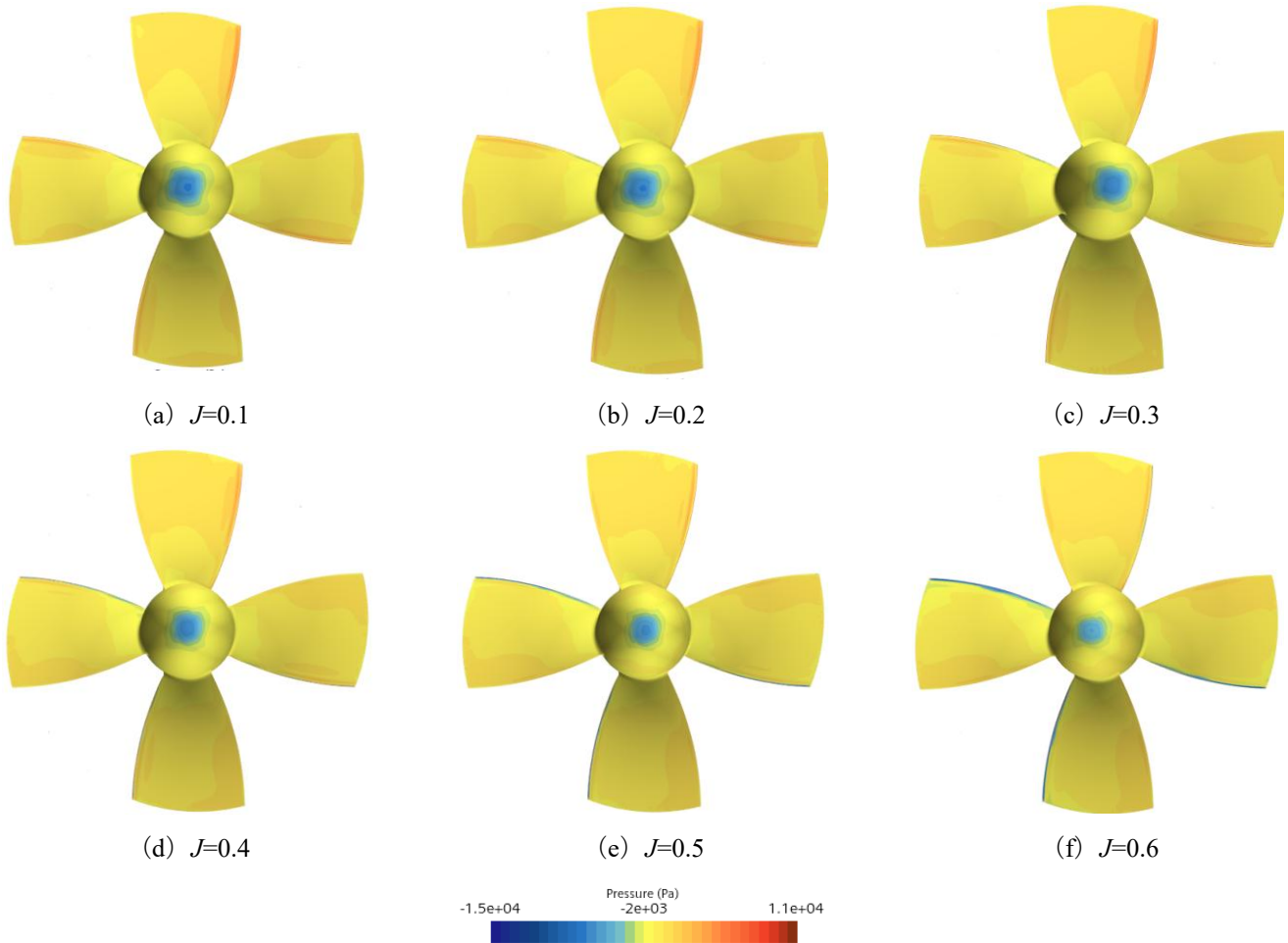


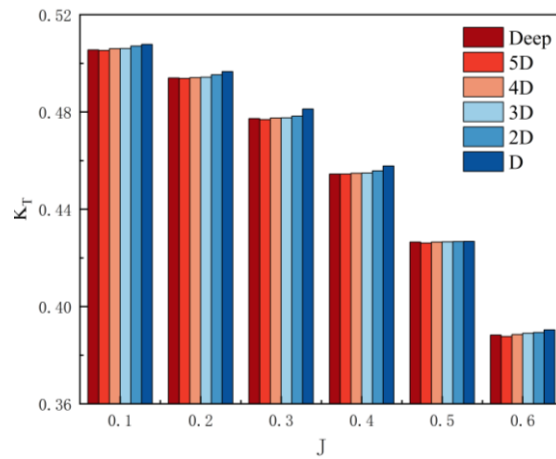
Fig. 12 Pressure distribution on blade face under different advance speeds

4. Influence of water depth on open water performance

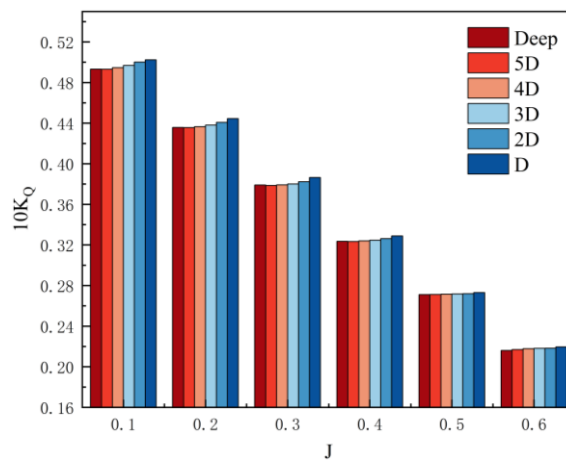
After verifying the reliability of the numerical calculation model, all other settings remain unchanged, and the boundary conditions at the bottom are set as a no-slip wall. In the calculation model, the distance between the center of the propeller disk and the bottom is denoted as H . Numerical models with H values of $5D$, $4D$, $3D$, $2D$, and D are subsequently computed in sequence.

According to the data under various water depth conditions in Figure 13 (a) to (c), it is observed that the curves of K_T , $10K_Q$ and η_0 with J exhibit different trends. As the water depth H decreases from deep water to $5D$, the K_T and $10K_Q$ of the propeller exhibit fluctuating trends of both increases and decreases, but the change range is very small, with average changes not exceeding 0.11 %. At the same time, due to the difference in the change range of K_T and $10K_Q$, the change trend of η_0 also increased or decreased. Overall, the shallow-water effect has little effect on the performance of the propeller when it is reduced from deep water to $5D$.

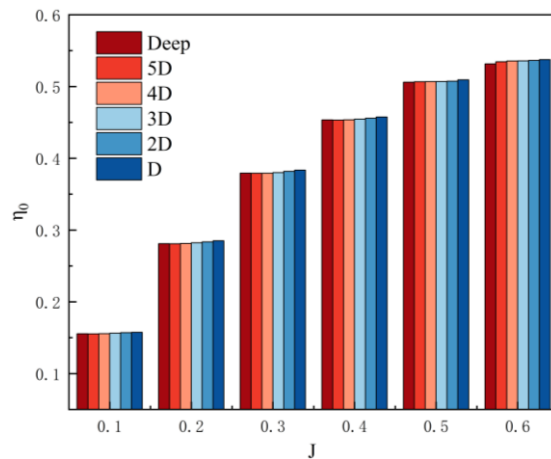
As the water depth further decreases from $5D$ to D , the K_T and $10K_Q$ and η_0 of the propeller all exhibit increasing trends. From $5D$ to D , the average variation ranges of K_T are 0.23 %, 0.24 %, 0.41 %, and 0.71 % respectively, the average variation ranges of $10K_Q$ are 0.115 %, 0.12 %, 0.14 %, and 0.29 % respectively, and the average variation ranges of η_0 are 0.11 %, 0.21 %, 0.30 %, and 0.38 % respectively, indicating that the influence of shallow-water effect on propeller performance is gradually enhanced. Notably, the increase of thrust coefficient K_T is significantly higher than that of torque coefficient $10K_Q$, which indicates that the thrust characteristics of propeller are more affected under shallow-water conditions. When the water depth decreases from $2D$ to D , the variation of the open water performance of the propeller increases significantly, and the influence of the shallow-water effect on the propeller is obviously enhanced. However, in general, the change of water depth has little effect on the performance of the propeller.



(a) K_T histogram



(b) K_Q histogram



(c) η_0 histogram

Fig. 13 Open water characteristic curves under different water depths

Figure 14 (a) to (f) and Figure 15 (a) to (f) are the pressure distribution of the propeller blade back and blade face when H is deep water, $5D$, $4D$, $3D$, $2D$, and D respectively at $J=0.2$. Comparing Figures 14 (a) to (f) and Figures 15 (a) to (f) respectively, the pressure distribution of blade back and blade face from deep water to $4D$ changes little with water depth. The pressure of the blade back and blade face from $3D$ to D decreases with deep water, and the pressure in the middle of the blade decreases obviously.

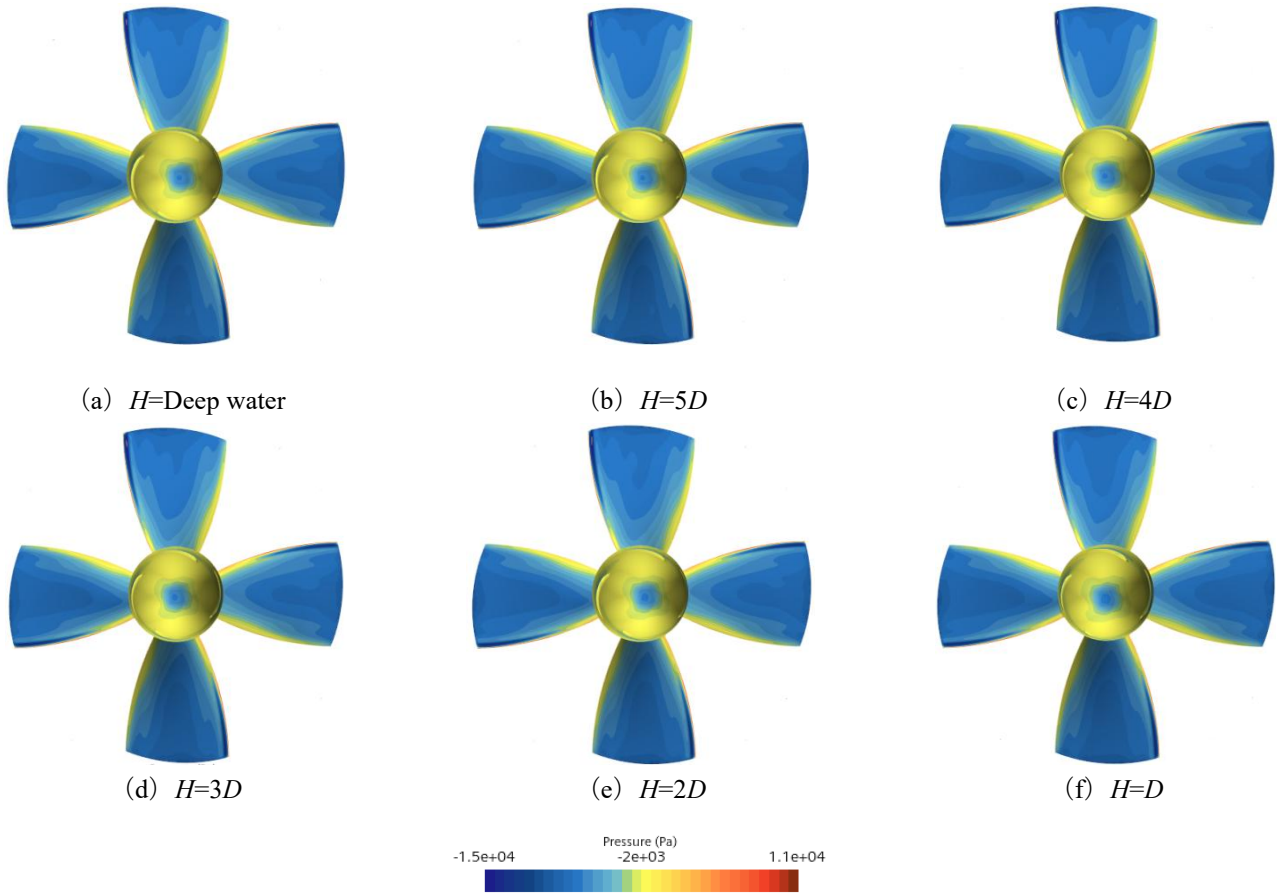


Fig. 14 Pressure distribution on blade back under different water depths

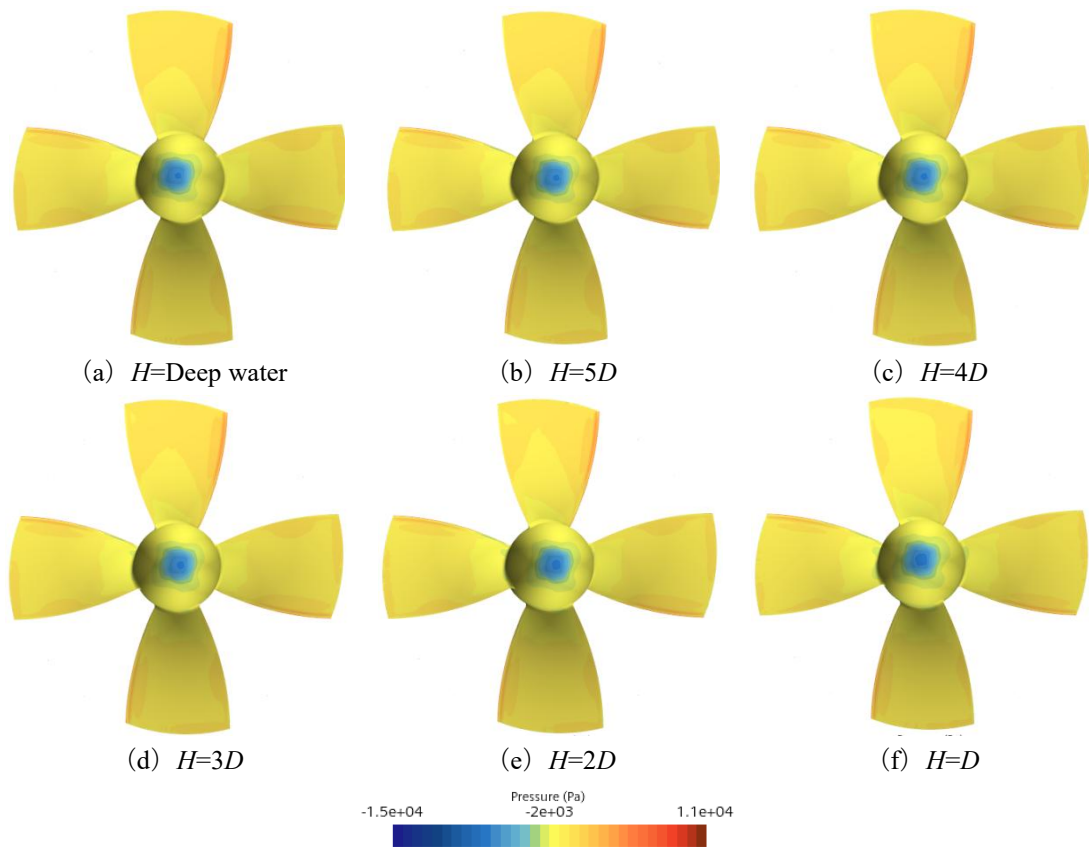


Fig. 15 Pressure distribution on blade face under different water depths

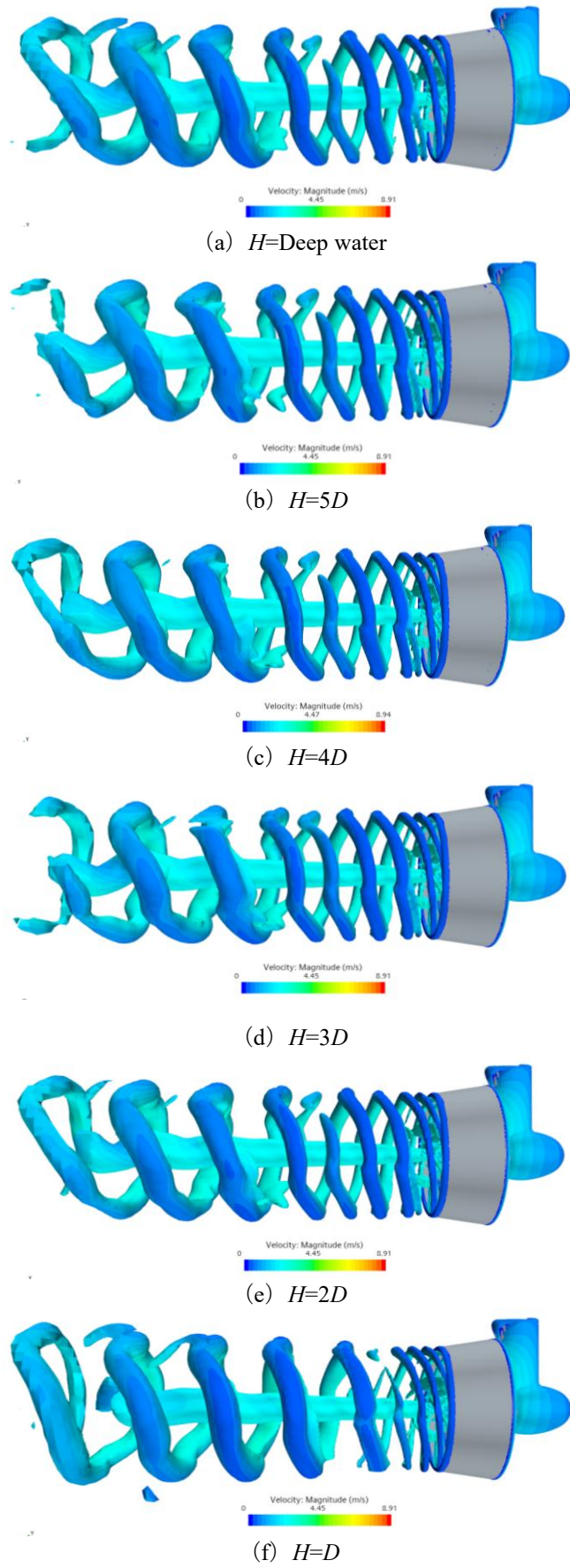
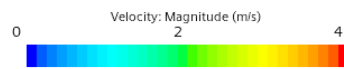
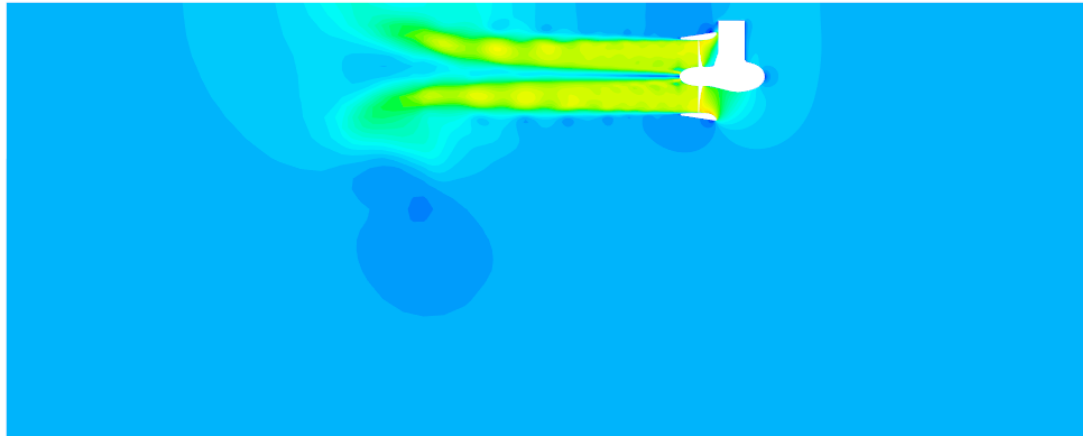


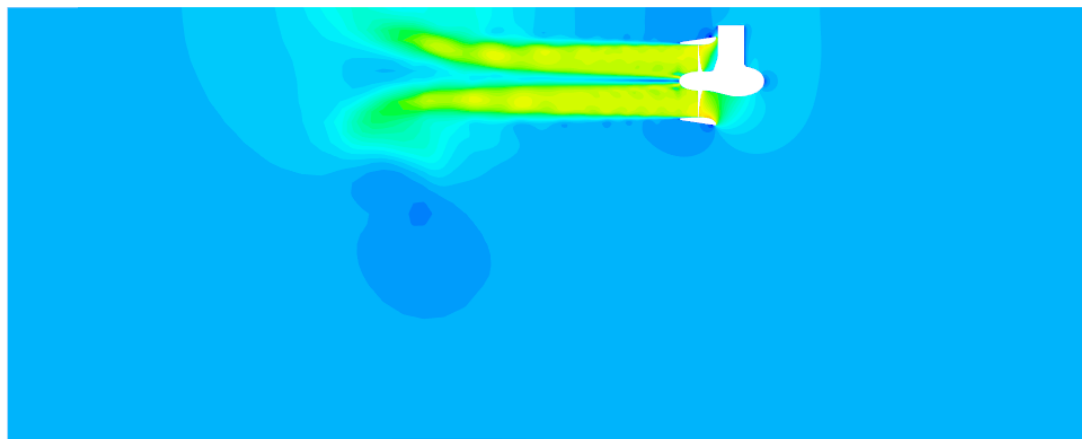
Fig. 16 Vortex structure under different water depths (based on Q criterion)

Figure 16 (a) to (f) depicts the vortex structures of the Z-drive ducted propeller. A variety of vortices can be observed, including the duct-induced vortices, hub vortex, blade trailing edge vortex, and tip-leakage vortex. Karman vortex street is formed near the propeller domain, and a stable annular vortex structure is also formed at the wall of the duct inlet.

As the water depth decreases, the vorticity change of H from deep water to $2D$ is not large, but the degree of breakage at the tail of the vortex tip is different, indicating that the propeller is less influence from shallow-water effects at this time. When the water depth is $H=D$, as illustrated in Figure 16(f), compared with deep water, the vorticity structure outside the duct is thinner and denser near the propeller and then becomes thicker and more distant, and the duct-induced vortex flow is enhanced. This is attributed to the restriction of vertical water movement by the water bottom, which alters the vorticity distribution, subsequently increasing the propeller load and leading to the collapse of the tip vortex.



(a) H =Deep water



(b) $H=5D$

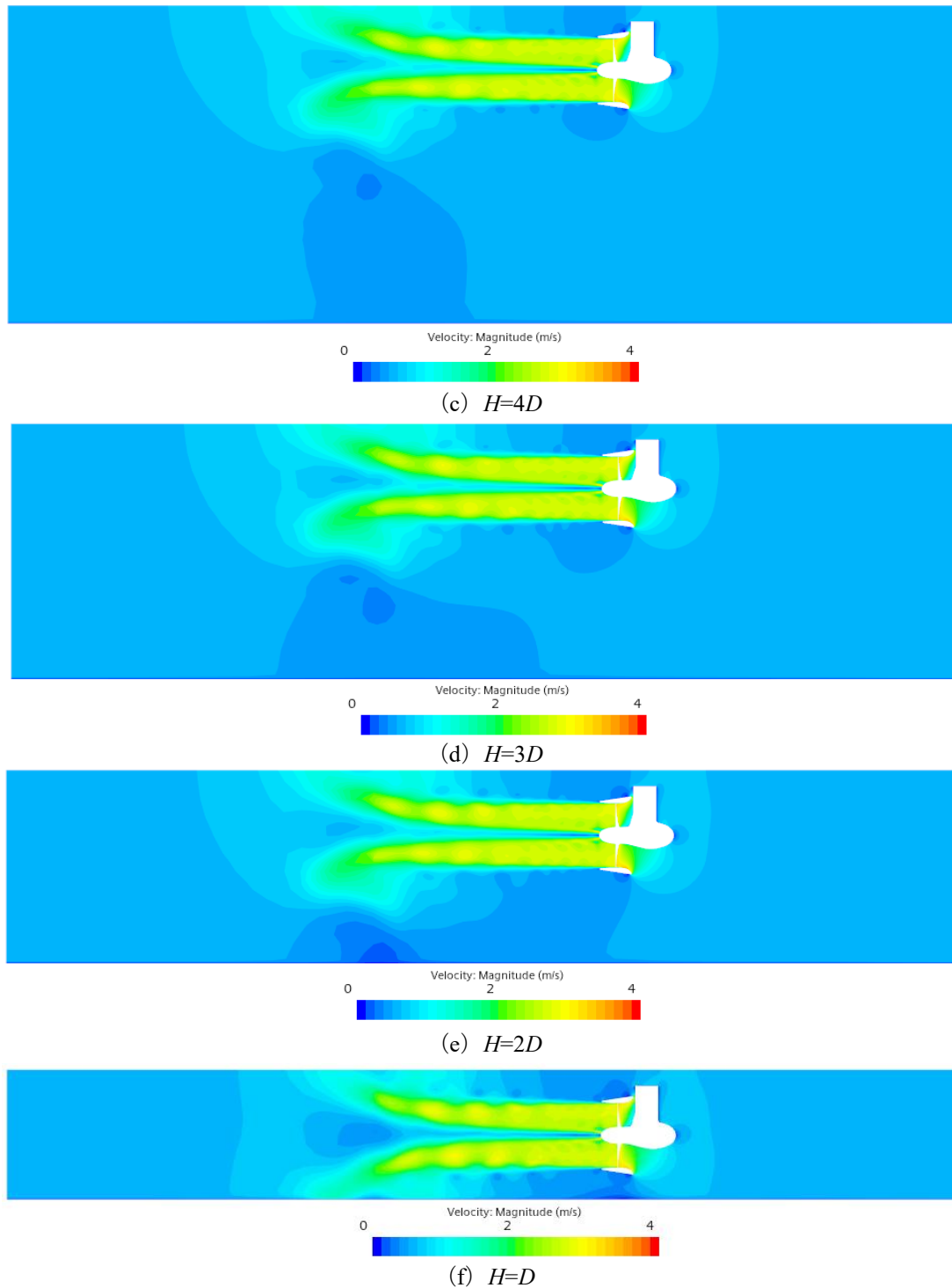


Fig. 17 The axial velocity distribution of flow field under different water depths

Figure 17 (a) to (f) is the axial velocity distribution of flow field on the longitudinal section of the propeller at $J=0.2$ and H is deep water, $5D$, $4D$, $3D$, $2D$ and D respectively. There is no obvious difference in the axial velocity distribution between the deep water and $H=D$, and only minor changes are observed in the flow field downstream due to the effects of the bottom wall. As the distance between the propeller and the water bottom decreases, the flow velocity increases when the water flows through the propeller, which will lead to a decrease of the pressure on the back of the propeller blade. Therefore, the total thrust of the propeller will increase. As the water flow velocity increases, the propeller experiences not only greater thrust but also heightened reaction forces and resistance. The increase of these forces makes the propeller torque increase accordingly, and the hydrodynamic performance of the propeller is also changing.

The axial flow field distribution contours from $H=5D$ to $H=D$ show that the flow velocity gradually increases around the propeller as water depth decreases, though the increase is not particularly pronounced. This is because the guiding effect of the rudder and the rectifying effect of the duct reduce the influence of the water depth on the flow field around the propeller to a certain extent. As water depth decreases, the velocity of the trailing wake gradually diminishes due to increased frictional resistance at the interface between the water flow and the water bottom.

In the range of water depths above $H=2D$, the impact of the seabed on the overall flow field around the propeller is relatively minor. However, when the water depth reaches $H=D$, the water bottom exerts a significant influence on the entire flow field. This is because the wall of the water bottom disturbs the trailing wake generated by the propeller, which in turn affects the distribution and performance of the flow field. Therefore, this provides valuable insights into the minimum operating water depth for the ship.

5. Conclusions

To fulfill the practical requirements of the propulsion system for the novel ship, the blades were designed using the Ka series propeller chart, resulting in a Ka+19A Z-drive ducted propeller that satisfied the needs of the ship. A comprehensive numerical analysis was conducted on the open water performance of this Z-drive ducted propeller under various water depth conditions. This study has provided valuable insights into the impact of shallow-water on propeller propulsion performance. According to the research results and in-depth analysis, the following conclusions are drawn:

A comparison between the numerical simulation results and the prototype experimental data for the Ka+19A Z-drive ducted propeller demonstrated strong agreement. The numerical simulation was conducted using a combination of the RANS method and the transient RBM method. It performed well in predicting the hydrodynamic performance of the Z-drive ducted propeller in shallow-water conditions and was capable of precisely capturing the complex flow field characteristics between the propeller and the water bottom.

Numerical research results indicated that when the water depth decreased from deep water conditions to $5D$, the shallow water effect had not yet manifested, and the open water performance of the Z-drive ducted propeller was largely unaffected. However, as the water depth further decreased to D , the shallow water effect began to become significant, which caused the $10K_Q$ and K_T of the Z-drive ducted propeller to show increasing trends. Notably, the increase in the K_T was greater than that of the $10K_Q$, this led to an increase in η_0 . When $H=D$, the open water performance results showed that the change rates of $10K_Q$, K_T , and η_0 compared with deep water conditions did not exceed 1.2 %, which indicated that the propeller was minimally affected by shallow-water effects.

From the vortex structure and axial velocity distribution of flow field of the Z-drive ducted propeller, it could be concluded that when the water depth H was from deep water to $2D$, the bottom wall had little effect on the vorticity and velocity wake field of the propeller. However, when the water depth $H=D$, the interference of the bottom wall on the propeller vorticity and wake field became significant. Consequently, to ensure normal operation of the Z-drive ducted propeller, it was recommended to set its operating water depth at $2D$ or deeper. The minimum operating depth of this ship was also not to be lower than the operationally suitable depth mentioned.

From the comparative analysis of the data, it could be deduced that although shallow-water had a certain impact on the hydrodynamic performance of the Z-drive ducted propeller, overall, the changes in the open water performance values, vorticity and flow field with varying water depths were not significant. This indicated that the Z-drive ducted propeller was minimally affected by shallow-water effects, which was advantageous for the propulsion efficiency of this novel ship in shallow areas, enabling it to operate effectively in such regions. Future research will continue to explore the self-propulsion hydrodynamic performance of this novel ship and its Z-drive ducted propeller, to further advance research and applications in this field.

REFERENCES

- [1] Bontempo, R., Manna, M., 2018. Performance analysis of ducted marine propellers. Part II - Accelerating duct. *Applied Ocean Research*, 75, 153-164. <https://doi.org/10.1016/j.apor.2018.03.005>
- [2] Andersson, J., Eslamdoost, A., Vikström, M., Bensow, R. E., 2018. Energy balance analysis of model-scale ship with open and ducted propeller configuration. *Ocean Engineering*, 167, 369-379. <https://doi.org/10.1016/j.oceaneng.2018.08.047>
- [3] Dai, Y., Zhang, Y. Y., Bian, J. N., Han, K., Zhu, X., Huang, Z. H., Xie, Y., 2021. CFD Simulation on Hydrodynamics of Underwater Vehicle with Ducted Propellers. *International Journal of Simulation Modelling*, 20(3), 595-605. <https://doi.org/10.2507/IJSIMM20-3-CO14>
- [4] Hoekstra, M., 2006. A Rans-Based analysis tool for ducted propeller systems in open water condition. *International Shipbuilding Progress*, 53(3), 205-227.
- [5] Bhattacharyya, A., Krasilnikov, V., Steen, S., 2016. A CFD-based scaling approach for ducted propellers. *Ocean Engineering*, 123, 116-30. <https://doi.org/10.1016/j.oceaneng.2016.06.011>
- [6] Jin, Z. H., Wang, P., Dong, H. C., An, X. Y., Xia, H., 2023. Numerical prediction of ducted propeller performance based on a Bem-Rans coupling method. *Ocean Engineering*, 271, 113761. <https://doi.org/10.1016/j.oceaneng.2023.113761>
- [7] Zhang, Z., Sun, P., Pan, L., Zhao, T., 2024. On the propeller wake evolution using large eddy simulations and physics-informed space-time decomposition. *Brodogradnja*, 75(1), 75102. <https://doi.org/10.21278/brod75102>
- [8] Go, J. S., Yoon, H. S., Jung, J. H., 2017. Effects of a duct before a propeller on propulsion performance. *Ocean Engineering*, 136, 54-66. <https://doi.org/10.1016/j.oceaneng.2017.03.012>
- [9] Stark, C., Shi, W. C., Altar, M., 2021. A numerical investigation into the influence of bio-inspired leading-edge tubercles on the hydrodynamic performance of a benchmark ducted propeller. *Ocean Engineering*, 237, 109593. <https://doi.org/10.1016/j.oceaneng.2021.109593>
- [10] Zhang, Q., Jaiman, R. K., 2018. Numerical analysis on the wake dynamics of a ducted propeller. *Ocean Engineering*, 171, 202-224. <https://doi.org/10.1016/j.oceaneng.2018.10.031>
- [11] Barrass, C. B., 2004. Chapter 18 - Reduced ship speed and decreased propeller revolutions in shallow-waters. *Ship Design and Performance for Masters and Mates*, 164-179. <https://doi.org/10.1016/B978-075066000-6/50020-9>
- [12] Nakisa, M., Behrouzi, F., Maimun, A., Samad, R., Ahmed, Y. M., 2017. Numerical Study on Propeller Performance for a ship in Restricted Water. *Procedia Engineering*, 194, 128-135. <https://doi.org/10.1016/j.proeng.2017.08.126>
- [13] Ma, Z.X., Ji, N., et al., 2024. Influence of scale effect on flow field offset for ships in confined waters. *Brodogradnja*, 75(1), 75106. <https://doi.org/10.21278/brod75106>
- [14] Liang, L., Hao, Z., Chaonan, Z., Jinbao, C., Baoji, Z., Xiangen, B., et al., 2024. Study on the effect of marine propeller wake on sediment siltation in a shallow-water channel. *Brodogradnja*, 75(3), 75106. <https://doi.org/10.21278/brod75308>
- [15] Su, S. J., Wu, Y. J., Xiong, Y. P., Guo, F. X., Liu, H. B., Cheng, Q. X., 2023. Experiment and numerical simulation study on resistance performance of the shallow-water seismic survey ship. *Ocean Engineering*, 279, 113889. <https://doi.org/10.1016/j.oceaneng.2023.113889>
- [16] Yurtseven, A., Aktay, K., 2023. The numerical investigation of spindle torque for a controllable pitch propeller in feathering maneuver. *Brodogradnja*, 74 (2), 95-108. <https://doi.org/10.21278/brod74205>
- [17] Eom, M. J., Jang, Y. H., Paik, K. J., 2021. A study on the propeller open water performance due to immersion depth and regular wave. *Ocean Engineering*, 219, 108265. <https://doi.org/10.1016/j.oceaneng.2020.108265>
- [18] Xia, H., Wang, P., Dong, H. C., Jin, Z. H., An, X. Y., Fang, L., 2022. Hydrodynamic characteristics of a new thrust vectoring ducted propeller with slotted nozzle. *Ocean Engineering*, 266(1), 112805. <https://doi.org/10.1016/j.oceaneng.2022.112805>
- [19] Han, S. Y., Wang, X. J., Wang, P., Dong, H. C., Jin, Z. H., 2023. Effects of blade tip thicknesses on hydrodynamic and noise performance of ducted propellers. *Ocean Engineering*, 289(2), 116270. <https://doi.org/10.1016/j.oceaneng.2023.116270>
- [20] Liu, B., Vanierschot, M., Buyschaert, F., 2022. Effects of transition turbulence modeling on the hydrodynamic performance prediction of a rim-driven thruster under different duct designs. *Ocean Engineering*, 256, 111142. <https://doi.org/10.1016/j.oceaneng.2022.111142>
- [21] Stern, F., Wilson, R. V., Coleman, H. W., Paterson, E. G., 2001. Comprehensive approach to verification and validation of CFD simulations—Part 1: Methodology and Procedures. *Journal of Fluids Engineering*, 123(4), 793-802. <https://doi.org/10.1115/1.1412235>
- [22] Wilson, R., Shao, J., Stern, F., 2004. Discussion: Criticisms of the “Correction Factor” Verification Method 1. *Journal of Fluids Engineering*, 126(4), 704-06. <https://doi.org/10.1115/1.1780171>
- [23] ITTC Procedures and Guidelines. P Uncertainty Analysis in CFD, Verification and Validation Methodology and Procedures, 2021. No. 7.5-03-01-01.
- [24] ITTC Recommended Procedures and Guidelines. Practical Guidelines for Ship CFD Applications, 2011. No. 7.5-03-02-03.

- [25] Jang, Y. H., Eom, M. J., Paik, K. J., Kim, S. H., Song, G., 2020. A numerical study on the open water performance of a propeller with sinusoidal pitch motion. *Brodogradnja*, 71(1), 71-83. <https://doi.org/10.21278/brod71105>
- [26] Nadery, A., Ghassemi, H., Chybowski, L., 2021. The effect of the PSS configuration on the hydrodynamic performance of the KP505 propeller behind the KCS. *Ocean Engineering*, 234, 109310. <https://doi.org/10.1016/j.oceaneng.2021.109310>
- [27] Ding, Y. L., Song, B. W., Wang, P., 2015. Numerical investigation of tip clearance effects on the performance of ducted propeller. *International Journal of Naval Architecture and Ocean Engineering*, 7(5), 795-804. <https://doi.org/10.1515/ijnaoc-2015-0056>